Transmission electron microscopy on live catalysts

Bremmer, G.M.

Chapter 4

Cobalt-rhenium β-Mn-type bimetallic nanoparticles prepared via colloidal chemistry

We report on the synthesis, thermal stability and structural evolution of β-manganese (Mn)-type cobalt (Co)–rhenium (Re) nanoparticles (NPs). Monodisperse $Co_{1-x}Re_x$ NPs are synthesized for the first time via a facile one-pot colloidal method, yielding excellent control of Re stoichiometry for $x \leq 0.15$. Scanning transmission electron microscopy–energy dispersive X-ray spectroscopy analysis demonstrates that the Re atoms are homogeneously distributed throughout the Co lattice. Synchrotron powder X-ray diffraction combined with Rietveld refinement shows clear preferential site occupancy of Re atoms in the 12-fold site. A maximum of 15 atom % Re can be incorporated into the Co lattice, yielding single-phase particles. *In situ* synchrotron powder X-ray diffraction heating studies show that in reducing atmosphere the β-Mn-type Co–Re NPs are stable up to 300 °C before transforming into hexagonal close-packed Co, implying Re segregation.

4.1 Introduction

Bimetallic nanoparticles (NPs) attract significant attention due to the immense technological potential that arises from size, morphology and compositional effects.[1-5] In catalytic processes, bimetallic NPs often exhibit superior performance compared to their monometallic counterparts.[6-8] The enhanced catalytic performance may originate from synergy between a modified electronic structure and the formation of new active sites, induced by the local presence of the second metallic element.[9,10] Co–Re NPs are of interest in catalytic processes such as the Fischer-Tropsch reaction and ammonia synthesis.[11-17] In the presence of small amounts of Re, the overall Fischer-Tropsch performance of Co in terms of activity and selectivity towards long-chain hydrocarbons (C_{5+}) is enhanced.[18-20] One long lasting debate, addressed both experimentally and theoretically, is the location of the Re promoter in the Co particles. While some studies indicate that Re is distributed inside the bulk Co matrix forming an alloy,[21] others propose that Re atoms accumulate on the surface in intimate contact with Co metal nanoparticles,[22] or that Re is located just below a surface consisting of Co atoms.[23] In these experimental studies,[21,22] the Co–Re bimetallic catalysts are prepared by wet impregnation, which gives limited control of parameters such as particle size and elemental distribution. A more targeted strategy would be the synthesis of free-standing Co–Re NPs via colloidal chemistry with subsequent deposition on a selected support material.[24-28] To the best of our knowledge, synthetic protocols for colloidal Co–Re NPs are currently unavailable. In this communication we report on a method to synthesize monodisperse Co–Re NPs with the β-Mn-type structure, a structure found for monometallic Co NPs.[29,30]

4.2 Experimental

4.2.1 Synthesis of Co-Re nanoparticles

Uniformly sized $Co_{1-x}Re_x$ ($x \leq 0.15$) NPs were synthesized by thermal decomposition of dicobalt octacarbonyl ($Co_2(CO)_8$, ≥ 90%) and dirhenium decacarbonyl ($Re_2(CO)_{10}$, 98%) metal precursors in ortho-dichlorobenzene (*o*-DCB, 99%, anhydrous) containing oleic acid (OA ≥ 99%) as stabilizing agent. All chemicals were purchased from Sigma-Aldrich and used without further purification.

For the synthesis of Co–Re NPs, the previously reported protocol for the synthesis of Co NPs [31] was subjected to various modifications (Figure 4.1). In a typical $Co_{0.85}Re_{0.15}$ NP synthesis, 0.20 mmol $Re_2(CO)_{10}$ and 65 µL OA (0.205 mmol) were dissolved in 15 mL *o*-DCB under Ar flow. The solution was subsequently heated to 177 ± 1 °C under stirring conditions. In the meantime, 1.11 mmol $Co_2(CO)_8$ was dissolved in 3 mL *o*-DCB in a glove box (O_2 and H_2O levels <1 ppm).

When the *o*-DCB/OA/$Re_2(CO)_{10}$ mixture reached the targeted temperature, the $Co_2(CO)_8$ precursor solution was rapidly injected into the hot mixture. The formed colloidal suspension was aged for 2–4 hours and subsequently quenched with 10 mL fresh *o*-DCB. The NPs were flocculated using excess 2-propanol and isolated by centrifugation. After discarding the supernatant, the NP precipitate was washed with 2-propanol for at least three times before redispersion in hexane. In order to tune the Co–Re metal composition, the relative amounts of Co and Re carbonyl precursors were systematically adjusted (Table 4.1).

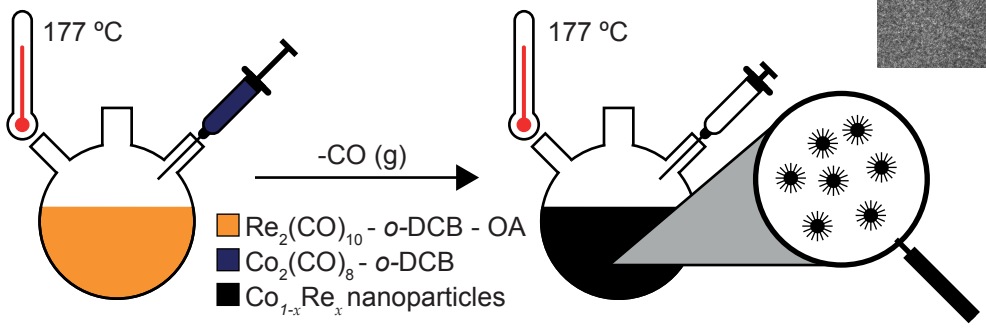

Figure 4.1. Colloidal Co–Re NPs formed via thermal decomposition of carbonyl precursors in the presence of OA as stabilizing agent and *o*-DCB as solvent.

Table 4.1. Amounts of reactants used for the preparation of $Co_{1-x}Re_x$ Nanoparticles.

	$Co_2(CO)_8$		$Re_2(CO)_{10}$		*o*-DCB	OA
Sample	mg	mmol	mg	mmol	mL	mmol
$Co_{0.97}Re_{0.03}$	440	1.286	28	0.043	18	0.205
$Co_{0.92}Re_{0.08}$	420	1.228	72	0.110	18	0.205
$Co_{0.85}Re_{0.15}$	380	1.111	132	0.202	18	0.205
$Co_{0.60}Re_{0.40}$	270	0.789	354	0.543	18	0.205

4.2.2 Nanoparticle characterization

The crystal structure and thermal stability of Co–Re NPs were investigated by synchrotron powder X-ray diffraction (SR-PXRD). All the experiments were performed at the Swiss-Norwegian Beamlines (SNBL), station BM01A, at the European Synchrotron Radiation Facility (ESRF). Diffraction profiles were collected using a PILATUS 2M detector. Wavelength (λ = 0.06957 nm) was calibrated by means of a NIST Si standard. For data reduction a PyFAI-based tool was used.[32] For structural investigations, dried samples were loaded (inside a glove box, O_2 and H_2O levels <1 ppm) in 0.7 mm diameter glass capillaries and sealed. Sets of diffraction patterns were collected at room temperature and the intensities were averaged to improve statistics. Rietveld refinements were performed using the Fullprof suite of programs [33] (2Θ range 10–37°; Δ2Θ = 0.0125°; 30 Bragg reflections, 10–13 variable parameters; manual background correction; typical Bragg R_F factor = 4.3, R_p = 10.4). For the temperature-dependent SR-PXRD experiments, an inhouse-made quartz capillary-based *in situ* cell was used. The $Co_{0.85}Re_{0.15}$ sample was loaded (inside a glove box) in a 0.7 mm diameter quartz capillary, with a bed length of ~10 mm, and kept in place by quartz wool plugs. Sample heating was provided by a vertical hot air blower. Flowing gas was supplied by a set of mass flow controllers calibrated for relatively small flows (~5 mL min^{-1}). A 4 vol. % H_2/He gas mixture (Messer Schweiz AG, 99.2%) was used. The sample was heated *in situ* over the temperature range 27 – 402 °C at a rate of 2 °C min^{-1}. The diffraction patterns were recorded simultaneously using a collection rate of 4 images min^{-1}.

High-resolution transmission electron microscopy (HRTEM) and scanning transmission electron microscopy (STEM) was performed using a Cs-corrected FEI Titan Cubed microscope operating at 300 kV, equipped with a Gatan US1000 2k x 2k CCD, a Direct Electron DE-12 4k x 3k CCD and a high-angle annular dark-field (HAADF) detector, or with a monochromated FEI Tecnai F20ST/STEM operating at 200 kV, equipped with a Gatan US4000 4k x 4x CCD. Both microscopes were equipped with an energy dispersive X-ray (EDX) detector (Oxford Instruments, X-MAX^N 100TLE Windowless) for EDX spectroscopy. Analysis of (STEM-)EDX data was done using AZTec software, version 3.1.

All TEM samples were prepared by drop casting 10 µL of the relevant NP dispersion onto ultrathin carbon film (< 3 nm) supported by lacey carbon film on 400 mesh copper grids (Ted Pella Inc.) and dried under inert atmosphere.

4.3 Results and discussion

4.3.1 Characterization of Co-Re nanoparticles

The NP composition was determined using HRTEM-EDX. Analysis of a number of single Co–Re NPs showed signals of both Co and Re, confirming their bimetallic nature. The average stoichiometries are summarized in Table 4.2 and Figure 4.2.

Table 4.2. Composition of Co-Re NPs, as determined by HRTEM-EDX.

Sample	Atom % Re[a]
$Co_{0.97}Re_{0.03}$	N.D.[b]
$Co_{0.92}Re_{0.08}$	5.1 ± 0.9
$Co_{0.85}Re_{0.15}$	12.2 ± 1.3

[a] Measurements on randomly selected single NPs, averaged.
[b] N.D. Not determined.

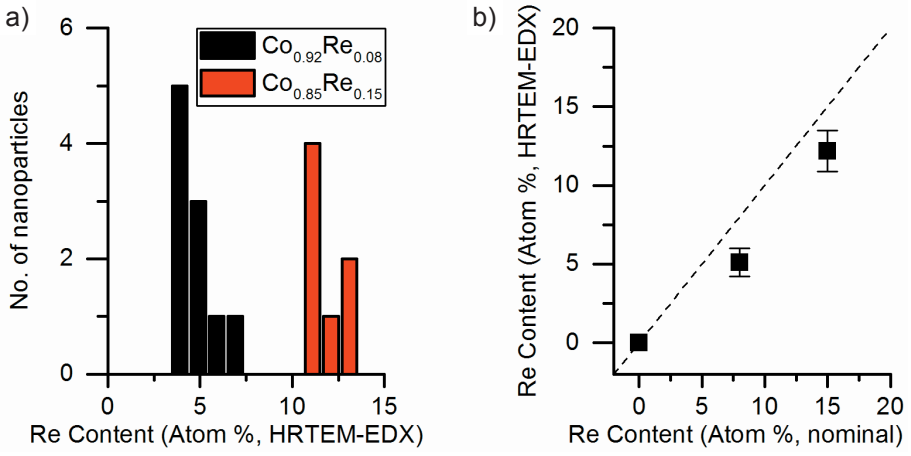

Figure 4.2. (a) Atomic composition as determined from HRTEM-EDX of $Co_{1-x}Re_x$ NPs on single nanoparticles. (b) Averaged composition (data points) determined by HRTEM-EDX versus nominal composition.

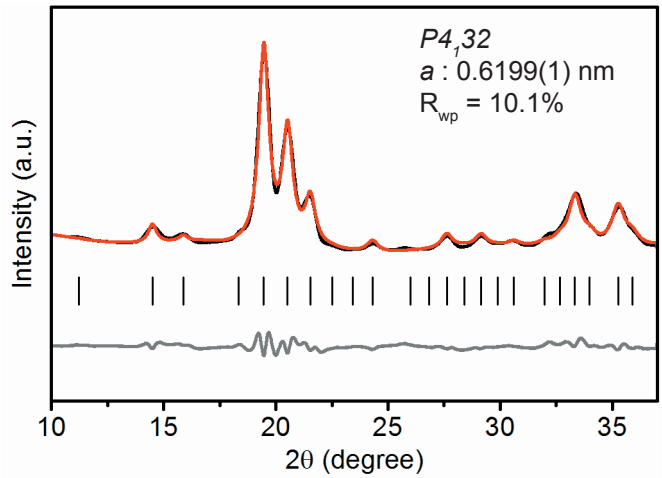

Figure 4.3. SR-PXRD pattern of $Co_{0.85}Re_{0.15}$ NPs (black) and corresponding Rietveld refinement. The calculated (red) and difference (gray) profiles are shown along with the positions for the Bragg reflections (vertical bars). λ = 0.06957 nm.

Figure 4.3 shows the SR-PXRD pattern of Co–Re NPs with nominal composition $Co_{0.85}Re_{0.15}$. Rietveld refinement using the structural model reported by Dinega and Bawendi [29] confirmed that the Co-Re NPs crystallize in the cubic *β*-Mn-type structure (space group $P4_132$). The refined crystallographic parameters are reported in Table 4.3. The Rietveld fit showed clear preferential site occupancy for Re-atoms in the 12-fold site.

Table 4.3. Crystallographic data[a] of *β*-Mn-type Co–Re NPs with nominal composition $Co_{0.85}Re_{0.15}$.

Species	Site	x	y	z	Occupancy
Co1 x,x,x	8*c*	0.0634(5)	0.0634(5)	0.0634(5)	0.666(1)
Re1 x,x,x	8*c*	0.0634(5)	0.0634(5)	0.0634(5)	0.000(1)
Co2 1/8,y,z	12*d*	0.125	0.193(2)	0.461(1)	0.818(7)
Re2 1/8,y,z	12*d*	0.125	0.193(2)	0.461(1)	0.182(7)

[a] T = 20 °C; Rwp = 10.1%; Space group: $P4_132$; Unit cell parameter, a = 0.6199(1) nm.

Figure 4.4 illustrates the moderate differences in the diffraction profiles depending on the Re-site distribution (Re at the 8-fold site; Re at the 12-fold site; random Co/Re distribution). For Co- or Mn-based bimetallic *β*-Mn-type solid solutions, both 8-fold and 12-fold site preferences have been reported.[33-35] Furthermore, it is evident that the unit cell expands upon Re incorporation. By assuming a linear relationship in the *a*-axis between the two end members Co and Re (*β*-Mn-type structure) [*a* = 0.6098(3) nm for Co [31]; and 0.697(2) nm for Re [36]] the refined value *a* = 0.6199(1) nm for the synthesized $Co_{0.85}Re_{0.15}$ NPs corresponds to a Re incorporation of 11.7 atom %. This value is in good agreement with the Re content (12.2 ± 1.3 atom %) determined by HRTEM-EDX (Table 4.2).

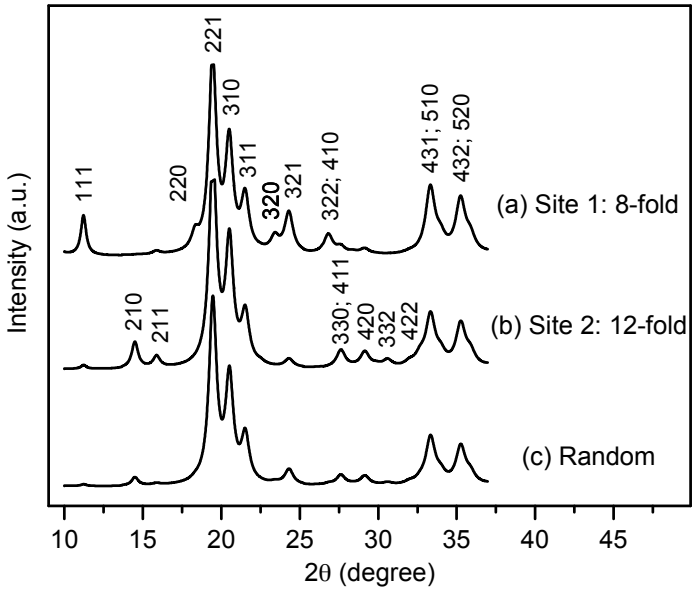

Figure 4.4. Calculated X-ray diffraction patterns of β-Mn-type Co–Re (Re, 1/6 fraction). In the simulated patterns, all Re atoms are assumed to occupy only (a) site 1 (8-fold); (b) site 2 (12-fold); or (c) are randomly distributed in the β-Mn-type Co lattice.

A representative high-angle annular dark-field scanning transmission electron microscopy (HAADF-STEM) image of the $Co_{0.85}Re_{0.15}$ NPs is shown in Figure 4.5a. The as-prepared particles have a spherical shape with an average diameter of 8 nm and a narrow size distribution (11% variation in diameter); as shown in Figure 4.5b.

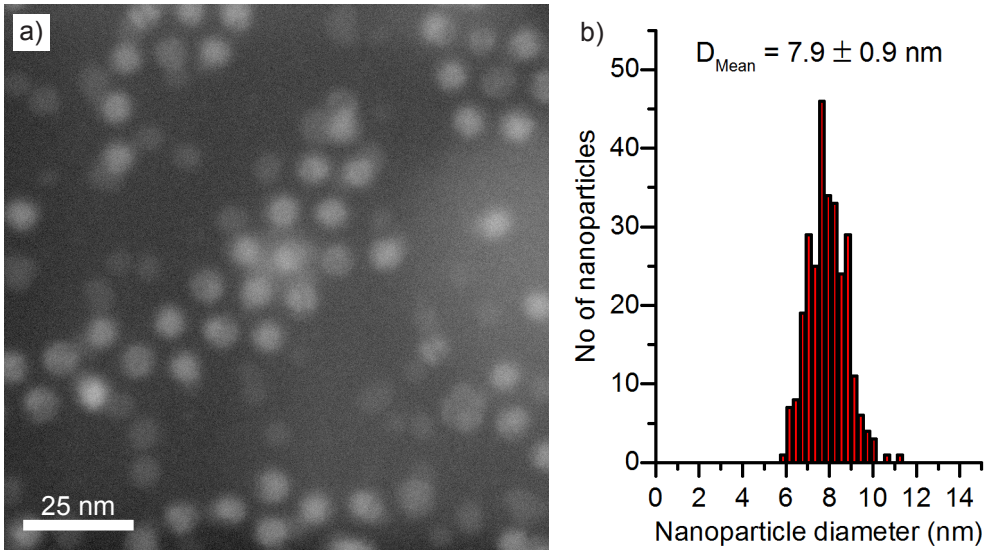

Figure 4.5. (a) HAADF-STEM image and (b) NP size distribution of $Co_{0.85}Re_{0.15}$ NPs.

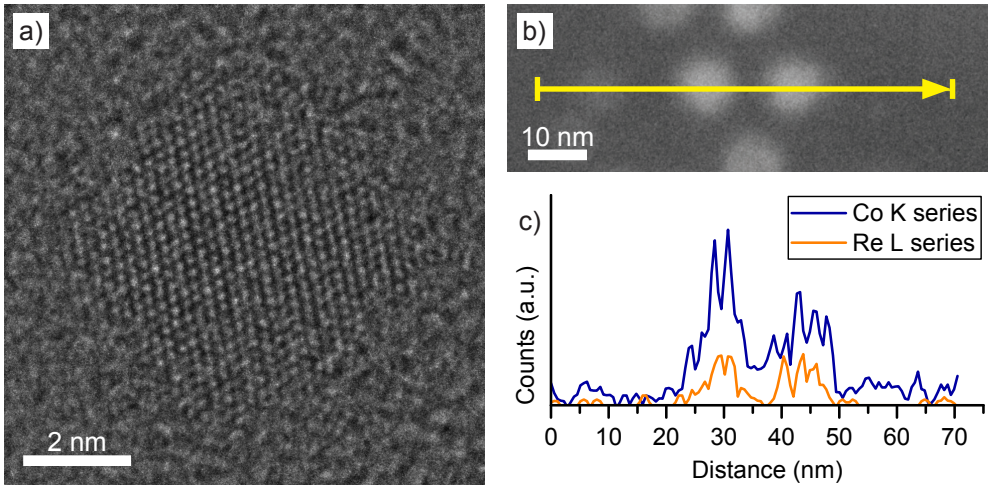

Figure 4.6. (a) HRTEM image of a single $Co_{0.85}Re_{0.15}$ nanoparticle. (b) HAADF-STEM image of multiple $Co_{0.85}Re_{0.15}$ NPs and (c) the corresponding STEM-EDX line scan profile recorded along the arrow direction.

HRTEM (Figure 4.6a) reveals homogeneous lattice fringes and a periodic lattice with no indications of Re segregation. To further investigate the elemental distribution in the individual NPs, STEM-EDX line scans were recorded (Figure 4.6b–c). The compositional line profiles across the two $Co_{0.85}Re_{0.15}$ NPs (Figure 4.6c) show homogeneous Co and Re distributions. These results indicate atomic-level mixing in the $Co_{0.85}Re_{0.15}$ crystallites. Based on SR-PXRD and STEM-EDX results, we conclude that the as-prepared $Co_{0.85}Re_{0.15}$ NPs form a solid solution.

4.3.2 Varying the Co-Re composition

Compositional tuning of the $Co_{1-x}Re_x$ ($x \leq 0.15$) NPs was achieved by adjusting the relative molar ratio between the two metal carbonyl precursors. Figure 4.7 shows the SR-PXRD patterns and Rietveld refinements of NPs with varying Re content. Careful inspection of the SR-PXRD patterns gave no indication for the existence of any crystalline phases with a high Re content; only Bragg reflections originating from the cubic β-Mn-type structure were identified.

For the $Co_{0.97}Re_{0.03}$ sample, SR-PXRD revealed some weak additional reflections (indicated by asterisk in Figure 4.7a). The origin of these reflections is not fully understood; however, possibly some can be related to hcp/ccp intergrowth particles. [31] It is worth mentioning that with increasing Re content (Figure 4.7b–c) the above mentioned reflections disappear, yielding single-phase particles.

Furthermore, an expansion in the a-axis with increasing Re content for $x \leq 0.15$ was observed for $Co_{1-x}Re_x$ (see Figure 4.8), in good agreement with what is expected from Vegard´s law approximation (dashed line).[37,38]

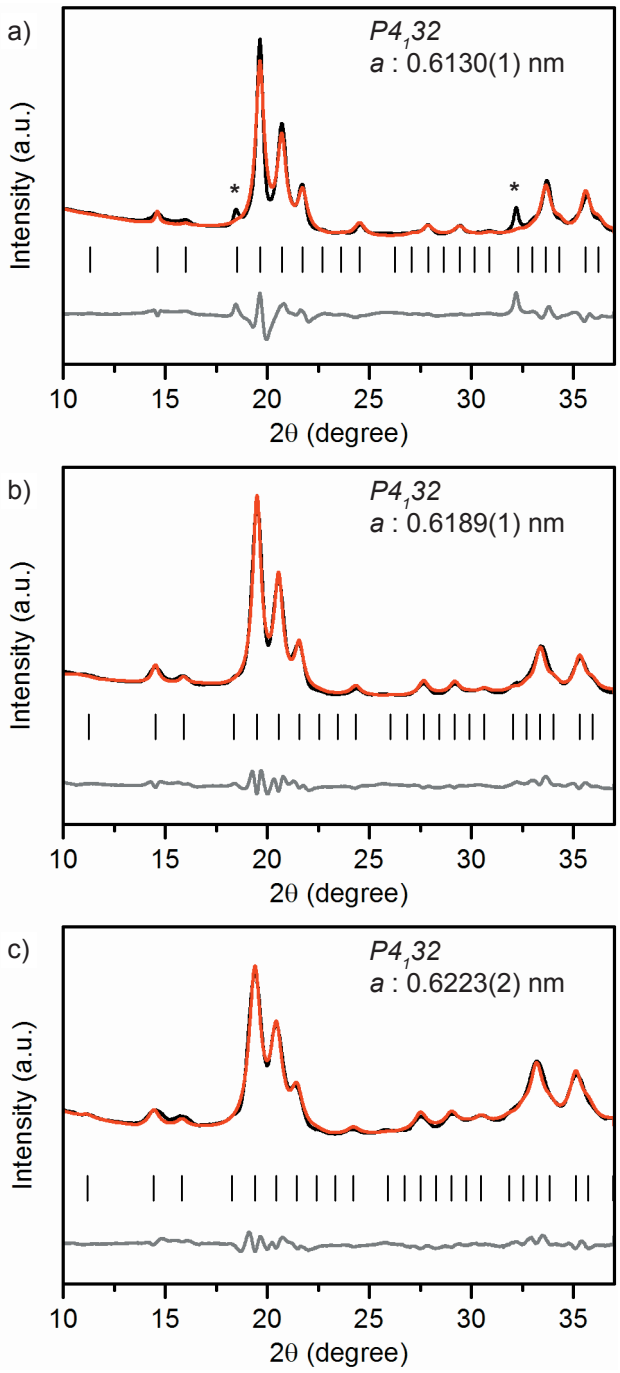

Figure 4.7. Rietveld refinements of synchrotron PXRD intensity profiles of a) $Co_{0.97}Re_{0.03}$; b) $Co_{0.92}Re_{0.08}$; and c) $Co_{0.60}Re_{0.40}$ NPs. Observed (black), calculated (red) and difference (gray) profiles are shown along with the positions for Bragg reflections (vertical bars). Impurity denoted with asterisk (*). λ = 0.06957 nm.

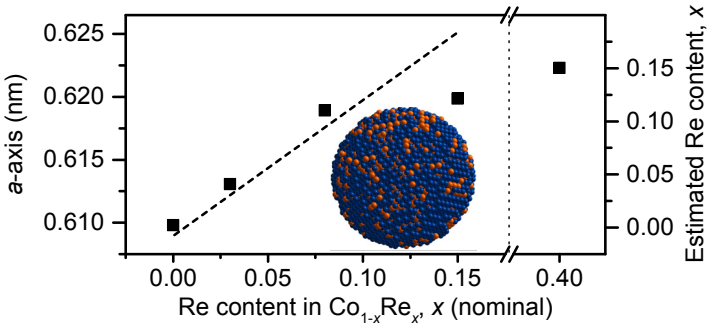

Figure 4.8. Refined *a*-axis (from SR-PXRD) versus nominal Re content for $Co_{1-x}Re_x$ NPs. Dashed line represents Vegard´s law linear relation. Estimated Re content (based on Vegard´s law) included on the right y-axis, along with a proposed graphical representation of the Co (blue) and Re (orange) atom distribution within the $Co_{1-x}Re_x$ particles ($x \leq 0.15$).

4.3.3 High Re content

However, we did not obtain uniform, single phased $Co_{1-x}Re_x$ NPs for $x > 0.15$. Attempts to synthesize such particles under our reaction conditions always resulted in a product with a Re content of ~15 atom %, as estimated from SR-PXRD. For example, SR-PXRD analysis of $Co_{0.60}Re_{0.40}$ gave a = 0.6223(1) nm (Figure 4.7c), corresponding to an estimated Re incorporation of 14.3 atom % (Figure 4.8).

While no other crystalline phases were detected by SR-PXRD, complementary TEM investigations of $Co_{0.60}Re_{0.40}$ revealed that the sample is highly inhomogeneous both with respect to particle size and chemical composition of the individual particles. Representative TEM images of the $Co_{0.60}Re_{0.40}$ NPs are presented in Figure 4.9. The particles are characterized by a tri-modal size distribution; the main population being spherical bimetallic Co–Re NPs with an average diameter of ca. 7 nm. Some ultra-small clusters and larger aggregates (with sizes of ~1 nm and 50–70 nm, respectively) were also identified. STEM-EDX mapping suggests that the latter are Re-rich (Figure 4.10). Our findings clearly suggest that within the explored experimental window, the solubility limit of Re into single-phased β-Mn-type Co NPs is ~15 atom %.

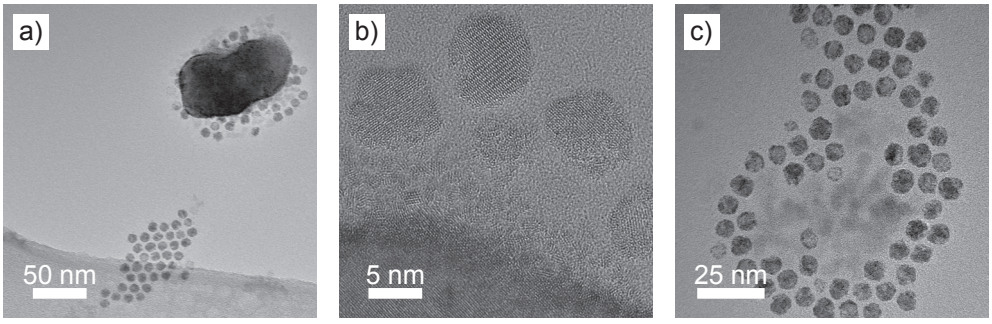

Figure 4.9. Representative TEM images of $Co_{0.60}Re_{0.40}$ on lacey carbon grid. (a) An ~80 nm-sized, Re-rich particle surrounded by Co-Re NPs. (b) High magnification image of a large Re-rich particle (bottom left corner) covered with ~1 nm clusters and a few Co-Re NPs of about 7 nm. (c) Cluster of Co-Re NPs of about 7 nm in size.

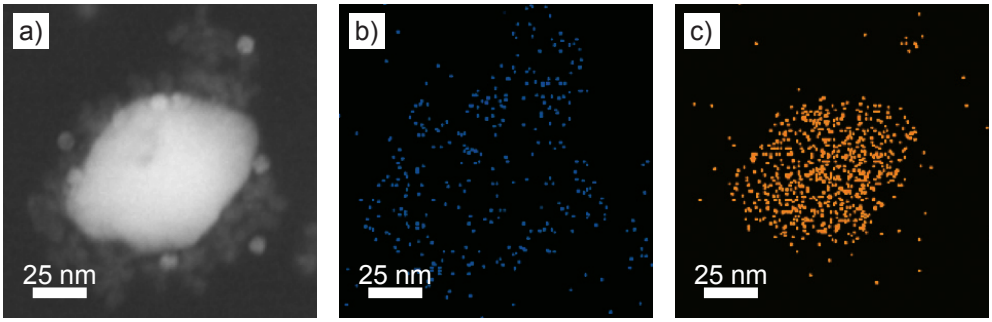

Figure 4.10. TEM images of the $Co_{0.60}Re_{0.40}$ sample on lacey carbon grid (a) HAADF-STEM image of a large Re-rich particle. (b) and (c) show the corresponding STEM-EDX mapping images of the Co K series (blue) and the Re L series (orange), respectively.

4.3.4 Thermal stability

The thermal stability of the β-Mn-type $Co_{0.85}Re_{0.15}$ NPs was studied by *in situ* SR-PXRD. Figure 4.11a shows a contour plot of the diffraction patterns from 27 – 402 °C upon heating in diluted H_2. Selected 2D-patterns are presented in Figure 4.11b. Upon heating, all Bragg reflections of the β-Mn-type phase are slightly shifting to lower angles due to thermal expansion (see e.g. the blue and cyan diffractograms at 204 and 286 °C, Figure 4.11b). For the β-Mn-type Co–Re NPs, the calculated linear thermal expansion coefficient in the temperature range of 100 – 250 °C is 25×10^{-6} $°C^{-1}$. Upon further heating, the NPs transform into a hexagonal close-packed (hcp) phase at around 300 °C (green and red diffractograms in Figure 4,11b). This phase transformation is in good agreement with reports on Co NPs.[30,39]

The sharp Bragg reflections of the hcp-type phase (red diffractogram at 349 °C, Figure 4.11b) clearly show that a complete recrystallization and particle growth process has taken place, with an estimated change from 5 to 30 nm sized crystallites (using the Scherrer equation) for the β-Mn and hcp-type phases, respectively. The calculated unit cell dimensions of the hcp-type phase at 349 °C are a = 0.2516 nm and c = 0.4095 nm. When using the thermal expansion coefficients of hcp Co (linear coefficients along the a and c axes; 12.5×10^{-6} $°C^{-1}$ and 17.8×10^{-6} $°C^{-1}$),[40] these values translate into a unit cell volume of 0.01105 nm^3/Co at 20 °C, which is very close to the value reported for pure hcp Co (0.01106 nm^3/Co).[41]

The high-temperature SR-PXRD data hence show that a drastic Re segregation occurs. The β-Mn-type Co–Re NPs transform into pure hcp Co, and consequently a separate high-Re-content phase forms, with too small particle size or to poor crystallinity to be detected by the applied method.

4.4 Conclusion

We report on the first synthesis of crystalline Co–Re NPs. According to Rietveld refinement these NPs take the β-Mn-type structure with a distinct site preference of Re atoms in the 12-fold site. Homogeneous elemental distribution of Co and Re in the individual NPs was further demonstrated using HRTEM and STEM-EDX line scans. The synthesized Co–Re NPs form a solid solution up to a maximum of

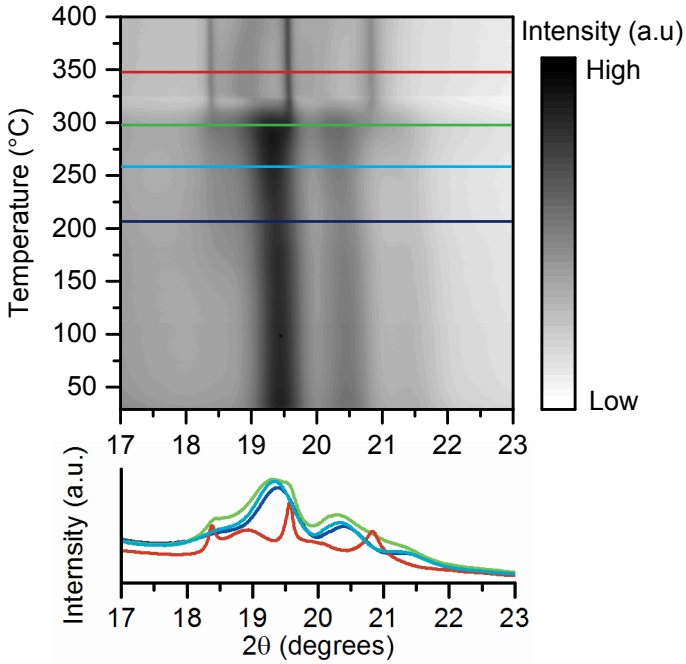

Figure 4.11. *In situ* synchrotron high temperature treatment of $Co_{0.85}Re_{0.15}$ NPs. (a) SR-PXRD contour plot upon heating in 4 vol. % H_2/He from 27 to 400 °C at a rate of 2 °C min^{-1}. (b) Selected 2D SR-PXRD patterns corresponding to the colored lines in (a). Blue = 204 °C, cyan = 256 °C, green = 298 °C, red = 349 °C. λ= 0.06957 nm.

~15 atom % Re. The thermal stability of the Co–Re NPs was explored in reducing atmosphere. The *β*-Mn polymorph is stable up to 300 °C, which defines the maximum operational temperature for this type of Co–Re NPs, a parameter of immense importance when utilized as nano-catalysts for industrial applications.

As the *β*-Mn-type Co–Re NPs are currently synthesized for the first time, their catalytic potential has not yet been explored. Although Co-containing Fischer-Tropsch catalysts are based on the hexagonal/cubic close-packed (hcp/ccp) Co polymorphs,[15, 42] currently no routes for controlled hcp/ccp Co–Re NPs synthesis exist. Therefore, the synthesis of *β*-Mn-type Co–Re NPs represents a promising possibility to obtain well-defined model catalysts.[24-28] These will be highly attractive for detailed investigations to elucidate the role of the Re promoter in the Co-based Fischer-Tropsch process. The *β*-Mn-type Co–Re NPs can be studied as such, or thermally converted into a hcp/ccp structure, which ought to be possible, yet is still very challenging.

References

[1] Ferrando, R.; Jellinek, J.; Johnston, R. L. Nanoalloys: From Theory to Applications of Alloy Clusters and Nanoparticles. *Chem. Rev.* **2008**, *108* (3), 845–910 DOI: 10.1021/cr040090g.

[2] You, H.; Yang, S.; Ding, B.; Yang, H. Synthesis of Colloidal Metal and Metal Alloy Nanoparticles for Electrochemical Energy Applications. *Chem. Soc. Rev.* **2013**, *42* (7), 2880–2904 DOI: 10.1039/C2CS35319A.

[3] Barcaro, G.; Caro, A.; Fortunelli, A. Springer Handbook of Nanomaterials; Editor: Vajtai, R.; Springer Berlin, Heidelberg, **2013**; pp 409–472 DOI: 10.1007/978-3-642-20595-8.

[4] Gilroy, K. D.; Ruditskiy, A.; Peng, H.-C.; Qin, D.; Xia, Y. Bimetallic Nanocrystals: Syntheses, Properties, and Applications. *Chem. Rev.* **2016**, *116* (18), 10414–10472 DOI: 10.1021/acs.chemrev.6b00211.

[5] Yan, Y.; Du, J. S.; Gilroy, K. D.; Yang, D.; Xia, Y.; Zhang, H. Intermetallic Nanocrystals: Syntheses and Catalytic Applications. *Adv. Mater.* **2017**, *29* (14), 1605997 DOI: 10.1002/adma.201605997.

[6] Nakamula, I.; Yamanoi, Y.; Imaoka, T.; Yamamoto, K.; Nishihara, H. A Uniform Bimetallic Rhodium/Iron Nanoparticle Catalyst for the Hydrogenation of Olefins and Nitroarenes. *Angew. Chem. Int. Ed.* **2011**, *50* (26), 5830–5833 DOI: 10.1002/anie.201102836.

[7] Zhang, S.; Metin, Ö.; Su, D.; Sun, S. Monodisperse AgPd Alloy Nanoparticles and Their Superior Catalysis for the Dehydrogenation of Formic Acid. *Angew. Chem. Int. Ed.* **2013**, *52* (13), 3681–3684 DOI: 10.1002/anie.201300276.

[8] Xia, B. Y.; Wu, H. B.; Li, N.; Yan, Y.; Lou, X. W. D.; Wang, X. One-Pot Synthesis of Pt-Co Alloy Nanowire Assemblies with Tunable Composition and Enhanced Electrocatalytic Properties. *Angew. Chem. Int. Ed.* **2015**, *54* (12), 3797–3801 DOI: 10.1002/anie.201411544.

[9] Alayoglu, S.; Eichhorn, B. Rh-Pt Bimetallic Catalysts: Synthesis, Characterization, and Catalysis of Core-Shell, Alloy, and Monometallic Nanoparticles. *J. Am. Chem. Soc.* **2008**, *130* (51), 17479–17486 DOI: 10.1021/ja8061425.

[10] Singh, A. K.; Xu, Q. Synergistic Catalysis Over Bimetallic Alloy Nanoparticles. *ChemCatChem*. **2013**, *5* (3), 652–676 DOI: 10.1002/cctc.201200591.

[11] Eri, S.; James G Goodwin, J.; Marcelin, G.; Riis, T. Catalyst for Production of Hydrocarbons. US Patent 4801573, **1989**.

[12] Behrmann, W. C.; Arcuri, K. B.; Mauldin, C. H. Surface Supported Cobalt Catalysts, Process Utilizing These Catalysts for the Preparation of Hydrocarbons From Synthesis Gas and Process for the Preparation of Said Catalysts. US Patent 5545674, **1996**.

[13] Espinoza, R. L.; Visagie, J. L.; Van Berge, P. J.; Bolder, F. H. Catalysts. US Patent 5733839, **1998**.

[14] Schanke, D.; Rytter, E.; Jaer, F. O. Scale-Up of Statoil's Fischer-Tropsch Process. In Natural Gas Conversion VII, Proceedings of the 7th Natural Gas Conversion Symposium; *Stud. Surf. Sci. Catal.* **2004**, *147*, 43–48 DOI: 10.1016/S0167-2991(04)80025-9.

[15] Tsakoumis, N. E.; Walmsley, J. C.; Rønning, M.; van Beek, W.; Rytter, E.; Holmen, A. Evaluation of Reoxidation Thresholds for γ-Al_2O_3-Supported Cobalt Catalysts Under Fischer-Tropsch Synthesis Conditions. *J. Am. Chem. Soc.* **2017**, *139* (10), 3706–3715 DOI: 10.1021/jacs.6b11872.

[16] Kojima, R.; Aika, K.-I. Rhenium Containing Binary Catalysts for Ammonia Synthesis. *Appl. Catal. A*, **2001**, *209* (1-2), 317–325 DOI: 10.1016/S0926-860X(00)00764-X.

[17] McAulay, K.; Hargreaves, J. S. J.; McFarlane, A. R.; Price, D. J.; Spencer, N. A.; Bion, N.; Can, F.; Richard, M.; Greer, H. F.; Zhou, W. Z. The Influence of Pre-Treatment Gas Mixture Upon the Ammonia Synthesis Activity of Co–Re Catalysts. *Catal. Comm.* **2015**, *68*, 53–57 DOI: 10.1016/j.catcom.2015.04.016.

[18] Bazin, D.; Borko, L.; Koppány, Z.; Kovács, I.; Stefler, G.; Sajó, L. I.; Schay, Z.; Guczi, L. Re-Co/NaY and Re-Co/Al_2O_3 Bimetallic Catalysts: *In Situ* EXAFS Study and Catalytic Activity. *Catal. Lett.* **2002**, *84* (3-4), 169–182 DOI: 10.1023/A:1021423802679.

[19] Martínez, A.; López, C.; Márquez, F.; Díaz, I. Fischer–Tropsch Synthesis of Hydrocarbons Over Mesoporous Co/SBA-15 Catalysts: the Influence of Metal Loading, Cobalt Precursor, and Promoters. *J. Catal.* **2003**, *220* (2), 486–499 DOI: 10.1016/S0021-9517(03)00289-6.

[20] Storsæter, S.; Borg, Ø.; Blekkan, E. A.; Holmen, A. Study of the Effect of Water on Fischer–Tropsch Synthesis Over Supported Cobalt Catalysts. *J. Catal.* **2005**, *231* (2), 405–419 DOI: 10.1016/j.jcat.2005.01.036.

[21] Voronov, A.; Tsakoumis, N. E.; Hammer, N.; van Beek, W.; Emerich, H.; Rønning, M. The State and Location of Re in Co–Re/Al_2O_3 Catalysts During Fischer–Tropsch Synthesis: Exploring High-Energy XAFS for *In Situ* Catalysts Characterisation. *Catal. Today* **2014**, *229*, 23–33 DOI: 10.1016/j.cattod.2013.11.069

[22] Jacobs, G.; Chaney, J. A.; Patterson, P. M.; Das, T. K.; Davis, B. H. Fischer–Tropsch Synthesis: Study of the Promotion of Re on the Reduction Property of Co/Al_2O_3 Catalysts by *In Situ* EXAFS/XANES of Co K and Re L_{III} Edges and XPS. *Appl. Catal. A*, **2004**, *264* (2), 203–212 DOI: 10.1016/j.apcata.2003.12.049

[23] Bakken, V.; Bergene, E.; Rytter, E.; Swang, O. Bimetallic Cobalt/Rhenium Systems: Preferred Position of Rhenium Through an Interdisciplinary Approach. *Catal. Lett.* **2010**, *135* (1-2), 21–25 DOI: 10.1007/s10562-009-0089-6.

[24] Somorjai, G. A.; Park, J. Y. Molecular Factors of Catalytic Selectivity. *Angew. Chem. Int. Ed.* **2008**, *47* (48), 9212–9228 DOI: 10.1002/anie.200803181.

[25] Jürgens, B.; Borchert, H.; Ahrenstorf, K.; Sonström, P.; Pretorius, A.; Schowalter, M.; Gries, K.; Zielasek, V.; Rosenauer, A.; Weller, H.; et al. Colloidally Prepared Nanoparticles for the Synthesis of Structurally Well-Defined and Highly Active Heterogeneous Catalysts. *Angew. Chem. Int. Ed.* **2008**, *47* (46), 8946–8949 DOI: 10.1002/anie.200802188.

[26] Jia, C.-J.; Schüth, F. Colloidal Metal Nanoparticles as a Component of Designed Catalyst. *Phys. Chem. Chem. Phys.* **2011**, *13* (7), 2457–2487 DOI: 10.1039/c0cp02680h.

[27] An, K.; Somorjai, G. A. Size and Shape Control of Metal Nanoparticles for Reaction Selectivity in Catalysis. *ChemCatChem*, **2012**, *4* (10), 1512–1524 DOI: 10.1002/

cctc.201200229.

[28] Na, K.; Zhang, Q.; Somorjai, G. A. Colloidal Metal Nanocatalysts: Synthesis, Characterization, and Catalytic Applications. *J. Clust. Sci.* **2014**, *25* (1), 83–114 DOI: 10.1007/s10876-013-0636-6.

[29] Dinega, D. P.; Bawendi, M. G. A Solution-Phase Chemical Approach to a New Crystal Structure of Cobalt. *Angew. Chem. Int. Ed.* **1999**, *38* (12), 1788–1791 DOI: 10.1002/(SICI)1521-3773(19990614)38:12<1788::AID-ANIE1788>3.0.CO;2-2.

[30] Sun, S.; Murray, C. B. Synthesis of Monodisperse Cobalt Nanocrystals and Their Assembly Into Magnetic Superlattices (Invited). *J. Appl. Phys.* **1999**, *85* (8), 4325 DOI: 10.1063/1.370357.

[31] Zacharaki, E.; Kalyva, M.; Fjellvåg, H.; Sjåstad, A. O. Burst Nucleation by Hot Injection for Size Controlled Synthesis of ε-Cobalt Nanoparticles. *Chem. Cent. J.* **2016**, *10* (1), 10 DOI: 10.1186/s13065-016-0156-1.

[32] Dyadkin, V.; Pattison, P.; Dmitriev, V.; Chernyshov, D. A New Multipurpose Diffractometer PILATUS@SNBL. *J. Synchrotron Rad.* **2016**, *23* (Pt 3), 825–829 DOI: 10.1107/S1600577516002411.

[33] Rodríguez-Carvajal, J. Recent Advances in Magnetic Structure Determination by Neutron Powder Diffraction. *Phys. B (Amsterdam, Neth.)* **1993**, *192* (1-2), 55–69 DOI: 10.1016/0921-4526(93)90108-I.

[34] Miyakawa, M.; Umetsu, R. Y.; Ohta, M.; Fujita, A.; Fukamichi, K.; Hori, T. Spin Fluctuation, Thermal Expansion Anomaly, and Pressure Effects on the Néel Temperature of β-MnM (M = Ru, Os, and Ir) Alloys. *Phys. Rev. B* **2005**, *72* (5), 054420 DOI: 10.1103/PhysRevB.72.054420.

[35] Karlsen, O. B.; Kjekshus, A.; Fjellvåg, H.; Ravindran, P.; Vidya, R.; Hauback, B. C. Structure and Magnetism of the β-Mn–Co Solid-Solution Phase. *J. Alloys Compd.* **2009**, *476* (1-2), 9–13 DOI: 10.1016/j.jallcom.2008.09.011.

[36] Xie, W.; Thimmaiah, S.; Lamsal, J.; Liu, J.; Heitmann, T. W.; Quirinale, D.; Goldman, A. I.; Pecharsky, V.; Miller, G. J. β-Mn-Type $Co_{(8+x)}Zn_{(12-x)}$ As a Defect Cubic Laves Phase: Site Preferences, Magnetism, and Electronic Structure. *Inorg. Chem.* **2013**, *52* (16), 9399–9408 DOI: 10.1021/ic4009653.

[37] Vavilova, V. V.; Galkin, L. N.; Glazov, M. V. Metastable Phase Formation Rules in Rhenium Based Alloys of Re-M System (M-Nb,Ta,Mo,W) During Fast Quenching. *Neorg. Mater.* **1991**, *27*, 2119–2123.

[38] Vegard, L. Die Konstitution Der Mischkristalle Und Die Raumfüllung Der Atome. *Z. Physik.* **1921**, *5* (1), 17–26 DOI: 10.1007/BF01349680.

[39] Denton, A.; Ashcroft, N. Vegard's Law. *Phys. Rev. A* **1991**, *43* (6), 3161–3164 DOI: 10.1103/PhysRevA.43.3161.

[40] Green, M. Organometallic Based Strategies for Metal Nanocrystal Synthesis. *Chem. Commun. (Camb.)* **2005**, *24*, 3002–3011 DOI: 10.1039/b501835h.

[41] Kasamatsu, Y.; Koyama, M.; Masumoto, K.-I.; Kojima, K.-I.; Hihara, T.; Kamigaichi, T. Dilatometric Measurement of the Thermal Expansion of Cobalt Single Crystal. *Jpn. J. Appl. Phys.* **1981**, *20* (1), 37–40 DOI: 10.1143/JJAP.20.37.

[42] Masumoto, H.; Watanabe, K.; Inagawa, K. O. N. Magnetic Properties of Hexagonal Close-Packed Structure Type Co–Ir Binary Alloys. *Trans. JIM* **1976**, *17* (9),

592–595 DOI: 10.2320/matertrans1960.17.592.

[43] Price, S. W. T.; Martin, D. J.; Parsons, A. D.; Sławiński, W. A.; Vamvakeros, A.; Keylock, S. J.; Beale, A. M.; Mosselmans, J. F. W. Chemical Imaging of Fischer-Tropsch Catalysts Under Operating Conditions. *Sci. Adv.* **2017**, *3* (3), e1602838 DOI: 10.1126/sciadv.1602838.